Frontiers of Information Technology & Electronic Engineering
www.jzus.zju.edu.cn; engineering.cae.cn; www.springerlink.com
ISSN 2095-9184 (print); ISSN 2095-9230 (online)
E-mail: jzus@zju.edu.cn

Hybrid near- and far-field three-stage beam training with beam split for RIS-assisted OFDM communications*

Zhichao CHENG[1], Shupei ZHANG[2], Shu FU[3], Boya DI‡[2]

[1]*School of Electronics Engineering and Computer Science, Peking University, Beijing 100871, China*
[2]*State Key Laboratory of Advanced Optical Communication Systems and Networks, School of Electronics, Peking University, Beijing 100871, China*
[3]*Department of Microelectronics and Communication Engineering, Chongqing University, Chongqing 400044, China*
E-mail: chengzhichao@stu.pku.edu.cn; zhangshupei@pku.edu.cn; shufu@cqu.edu.cn; diboya@pku.edu.cn

Received May 9, 2024; Revision accepted Oct. 21, 2024; Crosschecked Nov. 28, 2024

Abstract: With the development of millimeter-wave (mmWave) communication systems, large-scale reconfigurable intelligent surfaces (RISs) have gained considerable attention as a promising technology for signal strength enhancement and coverage extension. However, as the antenna scale and bandwidth increase, RIS-assisted wideband orthogonal frequency division multiplexing (OFDM) communication systems face challenges due to the near-field range expansion and the beam split effect over the high-frequency band, complicating the acquisition of channel state information (CSI). To tackle these challenges, we present a codebook-based three-stage beam training scheme by using the beam split effect to bypass CSI estimation. Specifically, by analyzing the beam split effect in RIS-assisted OFDM communication systems, we propose a beam-split-aware codebook capable of covering both the near and far fields with fewer codewords compared to conventional narrow-band codebooks. Using such a codebook, a three-stage beam training mechanism is adopted to obtain the optimal codeword with low time overhead, thereby facilitating subsequent beamforming. Simulation results demonstrate that the proposed scheme outperforms existing near- and far-field codebook-based schemes in terms of the beam training resolution and sum rate in the hybrid near–far field.

Key words: Near–far field; Beam split; Codebook design; Beam training; Reconfigurable intelligent surfaces
https://doi.org/10.1631/FITEE.2400372 **CLC number:** TN92

1 Introduction

With the rapid advancement of six-generation (6G) wireless mobile communication systems, millimeter-wave (mmWave) communication has garnered significant attention owing to its abundant bandwidth resources (Elayan et al., 2020; Ju et al., 2021). Although massive multiple-input multiple-output (MIMO) systems can achieve precise directional transmission, which is crucial for alleviating mmWave transmission attenuation issues, the expensive components of existing phased array antennas at mmWave bands, such as phase shifters, hinder their practical deployment and development (Wang X et al., 2018; Tariq et al., 2020; Zhang HB et al., 2022). Recently, reconfigurable intelligent surfaces (RISs), a novel type of artificial metamaterial (Cheng et al., 2023; Quan et al., 2023), offer a cost-effective alternative by intelligently reflecting signals to enhance reception strength (Shlezinger et al., 2019), which holds great potential in enabling efficient and reliable 6G communication systems (Basar et al., 2019; Tang et al., 2020; Yue et al., 2023).

To mitigate the high overhead of obtaining

‡ Corresponding author
* Project supported by the Natural Science Foundation of Beijing Municipality, China (Nos. QY23039, 4222005, and L212027) and the National Natural Science Foundation of China (Nos. 62322101, 62227809, and 62271012)
ORCID: Zhichao CHENG, https://orcid.org/0009-0000-9415-004X; Boya DI, https://orcid.org/0000-0003-3484-1361

accurate channel state information (CSI), codebook design and beam training are widely employed to offer efficient transmission schemes even in the absence of precise channel information (Wu W et al., 2020). However, new challenges have also arisen due to large antenna arrays and wide bandwidths. First, as the scale of the antenna increases and the operating frequency rises, the boundary between the near and far fields, e.g., the Rayleigh distance in classical electromagnetic (EM) theory, also expands (Yue et al., 2024). Such expansion leads to degraded performance of far-field codebooks based on the planar wave model (Liu YW et al., 2023). Second, the widening band exacerbates the beam split phenomenon in both the near and far fields, resulting in significant disparities in the beam directions across different subcarriers in orthogonal frequency division multiplexing (OFDM) systems (Wang BL et al., 2018). Consequently, this phenomenon may cause overlapping codeword coverage in conventional narrow-band codebooks, which can lead to errors in codeword selection during beam training, thereby reducing the beam training resolution and achievable data rates.

In the literature, existing works either focus on a narrow-band near–far field codebook design and beam training without considering the beam split effect (Zhang YP et al., 2022; Zhang YT et al., 2023; Wu CY et al., 2024) or rely on extra hardware components to deal with the frequency dependence in wideband systems (Cui et al., 2023; Gao et al., 2023). Within the realm of narrow-band near–far field research, Zhang YP et al. (2022) employed a two-phase beam training method across angular and distance domains for ultra-large-scale array communication systems, reducing the training overhead. For RIS-assisted communication systems, a layered codebook and beam training mechanism based on the near–far field were proposed (Zhang YT et al., 2023). To tackle the challenges posed by large bandwidth, Gao et al. (2023) introduced true time delay (TTD) to regulate the beam split phenomenon and optimize far-field beam training. Similarly, Cui et al. (2023) leveraged TTD and the beam split effect to reduce the overhead of near-field beam training.

Nevertheless, in RIS-assisted OFDM communication systems, near-field and far-field communication should be considered simultaneously. Meanwhile, it may not always be appropriate to introduce additional components due to hardware limitations and to preserve the cost and power efficiency advantages of the RIS (Chen YH et al., 2023). As such, it is crucial to develop a codebook design and beam training scheme suitable for RIS-assisted wideband OFDM communication systems.

In this paper, we aim to develop a codebook design and beam training scheme that leverages the beam split effect for RIS-assisted OFDM communication systems in the near–far field. The main contributions of this paper are summarized as follows:

1. We analyze the beam split effect in RIS-assisted OFDM communication systems. Using such an effect, we propose a codebook for wideband communications, which is capable of covering both the near and far fields with fewer codewords compared with existing narrow-band codebooks.

2. Based on the proposed beam-split-aware codebook, we propose a three-stage beam training mechanism to obtain the optimal codeword with low time overhead. By dividing the beam training process into multiple stages, it reduces the training overhead and mitigates the beam training error caused by the frequency-dependent channel gain.

3. Simulation results demonstrate the effectiveness of the proposed codebook design and beam training mechanism. Compared with existing near-field and far-field codebook-based beam training schemes, our proposed scheme performs better in terms of both beam training resolution and sum rate in the near–far field.

Notations: Scalars are denoted by italic letters; vectors and matrices are denoted by boldface lowercase and uppercase letters, respectively. For a complex-valued vector $\boldsymbol{x}$, the function diag($\boldsymbol{x}$) denotes a diagonal matrix whose diagonal elements are the corresponding elements in $\boldsymbol{x}$, and the expression $\boldsymbol{x} \oslash \boldsymbol{y}$ denotes that the elements in $\boldsymbol{x}$ and $\boldsymbol{y}$ are divided correspondingly. $\boldsymbol{x}^*$ and $\boldsymbol{x}^{\mathrm{T}}$ denote the conjugate and transpose of $\boldsymbol{x}$, respectively.

2 System model

In this section, we first introduce the RIS-assisted OFDM communication system, and then present the RIS and transmission models.

2.1 Scenario description

As illustrated in Fig. 1, we consider a wideband downlink system, where a base station (BS) equipped with M antennas serves a single-antenna user equipment (UE). By adopting time division multiple access (TDMA), the proposed beam training mechanism can be easily extended to multi-user scenarios, which will be shown in Section 5. Without loss of generality, we choose to present the system model with a typical single user to streamline the analysis (Chen YH et al., 2023; Cui et al., 2023; Wu CY et al., 2024). Due to the dynamic wireless environment, the link between the UE and the BS can be unstable or even fall into a complete outage (Yue et al., 2023). To solve this problem, we deploy a RIS to assist the communication, which is an N-element uniform linear array (ULA). The BS uses OFDM with K subcarriers to serve the UE. The bandwidth of the system is denoted as B.

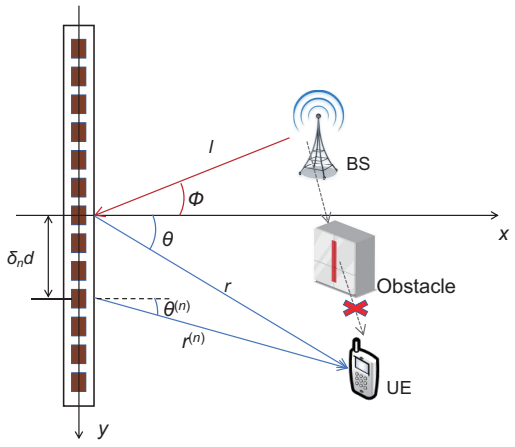

Fig. 1 RIS-assisted communication system (BS: base station; UE: user equipment)

2.2 RIS model

The RIS is composed of N reflective elements, each of which is a sub-wavelength metamaterial particle connected by multiple electrically controllable PIN diodes (Wu QQ and Zhang, 2020). By setting biased voltages applied to the PIN diodes, the RIS element can reflect the incident signal with a frequency-independent phase shift accordingly (Liu YW et al., 2021). Let Γ_n represent the reflection coefficient and φ_n the phase shift of the n^{th} RIS element. Then, the response matrix $\boldsymbol{Q}$ of the RIS array to the incident EM waves can be expressed as

$$\boldsymbol{Q}=\mathrm{diag}\left(\Gamma_1 \mathrm{e}^{\mathrm{j}\varphi_1},\Gamma_2 \mathrm{e}^{\mathrm{j}\varphi_2},\ldots,\Gamma_N \mathrm{e}^{\mathrm{j}\varphi_N}\right), \tag{1}$$

where $\varphi_n\in[0,2\pi)$ for all $n=1,2,\ldots,N$. For simplicity, we assume that φ_n can take continuous values in $[0,2\pi)$ and Γ_n equals 1 for all n from 1 to N.

2.3 Transmission model

As shown in Fig. 1, assuming that the UE is located at $(r\cos\theta, r\sin\theta)$, the general multipath downlink channel at the k^{th} subcarrier between the UE and RIS can be modeled as (Shi et al., 2024; Zhang YP and You, 2024)

$$\begin{aligned}\boldsymbol{h}_{\mathrm{ru}}[k]=&\sqrt{\frac{\kappa}{\kappa+1}}\boldsymbol{h}_{\mathrm{ru,LoS}}[k]\\&+\sqrt{\frac{1}{\kappa+1}}\sum_{l=1}^{L_{\mathrm{NLoS}}}\boldsymbol{h}_{\mathrm{ru,NLoS}}^{(l)}[k],\end{aligned} \tag{2}$$

where κ is the Rician factor. $\boldsymbol{h}_{\mathrm{ru,LoS}}$ and $\boldsymbol{h}_{\mathrm{ru,NLoS}}^{(l)}$ denote the line-of-sight (LoS) channel and the l^{th} non-LoS (NLoS) channel, respectively. The number of NLoS paths is represented as L_{NLoS}.

Due to the directional reflections of the RIS and severe loss incurred by scattering, the LoS link is typically stronger than other multipaths in mmWave communications (Piesiewicz et al., 2007). Therefore, in the remainder of this paper, we focus mainly on the LoS channel path. Based on the spherical wave assumption, the n^{th} element of $\boldsymbol{h}_{\mathrm{ru,LoS}}$ can be expressed as

$$h_{\mathrm{ru,LoS}}^{(n)}[k]=g_{\mathrm{ru}}[k]\mathrm{e}^{-\mathrm{j}\frac{2\pi f_k}{c}r^{(n)}}, \tag{3}$$

where $f_k=f_{\mathrm{c}}+\frac{B}{K-1}(k-1-\frac{K-1}{2})$ is the frequency of the k^{th} subcarrier with f_{c} denoting the central frequency of the system, and $g_{\mathrm{ru}}[k]$ denotes the complex path gain at frequency f_k. Without loss of generality, in this paper we assume that the channel gains $g_{\mathrm{ru}}[k]$ of different frequency subcarriers are independent of each other (Boljanovic et al., 2021). The term $r^{(n)}$ represents the distance from the UE to the n^{th} RIS element, which is given by

$$\begin{aligned}r^{(n)}&=\sqrt{r^2-2r\delta_n d\sin\theta+\delta_n^2 d^2}\\&\overset{\text{(a)}}{\approx} r-\delta_n d\sin\theta+\frac{\delta_n^2 d^2(1-\sin^2\theta)}{2r}\\&\overset{\text{(b)}}{=} r-\delta_n d\psi_{\mathrm{ue}}+\delta_n^2 d^2\mu_{\mathrm{ue}},\end{aligned} \tag{4}$$

where approximation (a) is based on the Fresnel approximation (Sherman, 1962). When $r > r_{\min} = 0.5\sqrt{\frac{D^3 f_c}{c}}$, where D represents the antenna aperture, the Fresnel approximation is accurate (Selvan and Janaswamy, 2017). Transformation (b) is obtained by defining $\psi_{\mathrm{ue}} = \sin\theta$ and $\mu_{\mathrm{ue}} = \frac{1-\sin^2\theta}{2r}$. The coordinates of the n^{th} RIS element are expressed as $(0, \delta_n d)$ with $\delta_n = \frac{2n-N-1}{2}$ $(n = 1, 2, \ldots, N)$, where $d = \frac{c}{2f_c}$ is the element spacing. Then the LoS channel of the RIS–UE link at the k^{th} subcarrier $\boldsymbol{h}_{\mathrm{ru,LoS}}[k]$ and the near-field steering vector $\boldsymbol{a}$ can be written as

$$\boldsymbol{h}_{\mathrm{ru,LoS}}[k] = g_{\mathrm{ru}}[k]\mathrm{e}^{-\mathrm{j}\frac{2\pi f_k}{c}r}\boldsymbol{a}(\psi_{\mathrm{ue}}, \mu_{\mathrm{ue}}, f_k), \tag{5}$$

$$\boldsymbol{a}(\psi, \mu, f) = \frac{1}{\sqrt{N}}[1, \mathrm{e}^{-\mathrm{j}2\pi\frac{f}{c}(r^{(1)}-r)}, \ldots, \mathrm{e}^{-\mathrm{j}2\pi\frac{f}{c}(r^{(N)}-r)}]^{\mathrm{T}}. \tag{6}$$

Considering that the BS antenna size is often much smaller than the RIS antenna size and the distance between them, we assume that the RIS is located in the far-field region of the BS (Yang et al., 2024). When the BS is located at $(l\cos\phi, l\sin\phi)$, the downlink channel at the k^{th} subcarrier between the BS and the RIS $\boldsymbol{H}_{\mathrm{br}}[k] \in \mathbb{C}^{N\times M}$ can be modeled as (Wu CY et al., 2024; Yang et al., 2024)

$$\boldsymbol{H}_{\mathrm{br}}[k] = g_{\mathrm{br}}[k]\boldsymbol{a}(\psi_{\mathrm{bs}}, \mu_{\mathrm{bs}}, f_k)\boldsymbol{b}^{\mathrm{T}}(\vartheta, f_k), \tag{7}$$

where $\psi_{\mathrm{bs}} = \sin\phi$, $\mu_{\mathrm{bs}} = \frac{1-\sin^2\phi}{2l}$, and ϑ is the spatial angle-of-departure (AoD) from the BS antennas to the RIS. The path gain between the BS and the RIS is represented as $g_{\mathrm{br}}[k]$. The term $\boldsymbol{b}$ denotes the far-field steering vector, given by

$$\boldsymbol{b}(\vartheta, f) = \frac{1}{\sqrt{M}}[1, \mathrm{e}^{-\mathrm{j}2\pi\frac{f}{c}d\vartheta}, \ldots, \mathrm{e}^{-\mathrm{j}2\pi\frac{f}{c}(M-1)d\vartheta}]. \tag{8}$$

As shown in Fig. 2, let $s[k]$ be the transmitted symbol at the k^{th} subcarrier. The BS first precodes $s[k]$ using a digital beamformer $\boldsymbol{v}_{\mathrm{D}}[k]$, where $\mathrm{Tr}(\boldsymbol{v}_{\mathrm{D}}[k]\boldsymbol{v}_{\mathrm{D}}^{\mathrm{H}}[k]) \le p[k]$, with $p[k]$ representing the transmit power allocated to the k^{th} subcarrier. Then, the processed signal is transformed to the time domain employing a K-point inverse discrete Fourier transform (IDFT). The signal in the time domain is then added the cyclic prefix (CP) to construct the transmitted signal (Chen Z et al., 2022). At the receiver side, the signal is first received by the UE antenna. Then, the CP is removed and the K-point discrete Fourier transform (DFT) is applied to recover the frequency-domain signal. Accordingly, the received signal $y[k]$ at the k^{th} subcarrier at the UE can be presented as

$$y[k] = \boldsymbol{h}_{\mathrm{ru}}^{\mathrm{T}}[k]\boldsymbol{Q}\boldsymbol{H}_{\mathrm{br}}[k]\boldsymbol{v}_{\mathrm{D}}[k]s[k] + n[k], \tag{9}$$

where $n[k]$ denotes the additive white Gaussian noise at the k^{th} subcarrier, obeying a Gaussian distribution $\mathcal{CN}(0, \sigma^2)$ with noise power σ^2. Note that existing algorithms for addressing carrier frequency offset, phase noise (Salim et al., 2014), and impulse noise (Suraweera and Armstrong, 2004) are applicable to codebook-assisted OFDM systems. Therefore, the proposed scheme can be applied in scenarios affected by these impairments.

3 Beam split analysis and key ideas

In this section, we first analyze the beam split effect of RIS-assisted OFDM communication systems in the near–far field, and then present key ideas for codebook design and beam training based on the analysis.

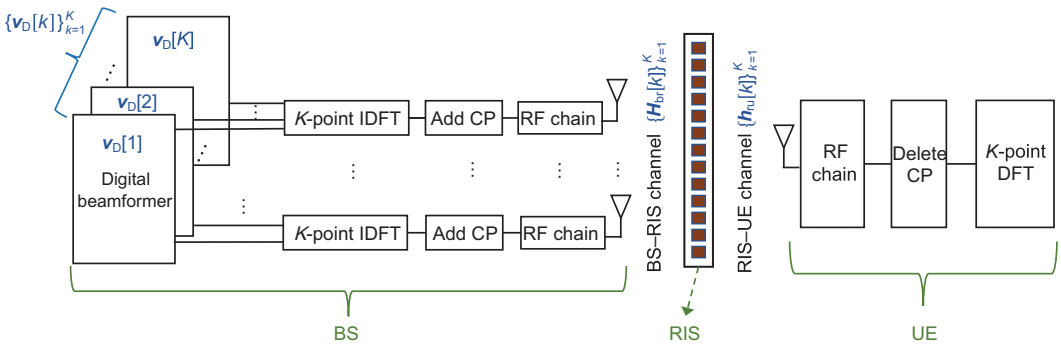

Fig. 2 Schematic of the transmission model in the RIS-assisted communication system (BS: base station; CP: cyclic prefix; DFT: discrete Fourier transform; IDFT: inverse DFT; RF: radio frequency; UE: user equipment)

3.1 Beam split in RIS-assisted OFDM communication systems

Now we analyze the beam split effect of RIS-assisted OFDM communication systems. In the following analysis, as mentioned in Section 2, we focus on the LoS channel path in which the BS–UE channel can be approximated as $\boldsymbol{h}_{\mathrm{ru}}[k] \approx \boldsymbol{h}_{\mathrm{ru,LoS}}[k]$ $(k=1,2,\ldots,K)$ (Zhang YP and You, 2024). Upon observing the expression of $\boldsymbol{a}$ in Eq. (6), we note that the steering vectors of wideband channels are frequency-dependent, whereas conventional phased array antennas can provide only frequency-independent phase shifts. This mismatch results in the beams generated by the phased array at different frequencies being focused on different locations, giving rise to the beam split phenomenon (Cui et al., 2023).

However, due to the additional wireless links introduced by the RIS, existing analysis of the beam split effect for traditional MIMO systems without considering the metasurface cannot be directly applied to RIS-assisted communication systems. Thus, we derive the specific formulation of the beam split effect of RIS-assisted OFDM communication systems in the near–far field, as detailed in Lemma 1.

Lemma 1 Assume that the BS position in the $\psi-\mu$ domain is at $(\psi_{\mathrm{bs}},\mu_{\mathrm{bs}})$, and that the spatial AoD from the BS antennas to the RIS is ϑ. When designing the BS digital beamformer to align with the BS–RIS channel and configuring the RIS such that the beam corresponding to the central frequency f_{c} is directed to $(\psi^{(\mathrm{c})},\mu^{(\mathrm{c})})$, the beam at frequency f_k is focused on the location (ψ_k,μ_k), expressed by

$$\psi_k=\frac{f_{\mathrm{c}}}{f_k}(\psi^{(\mathrm{c})}+\psi_{\mathrm{bs}})-\psi_{\mathrm{bs}}=\frac{f_{\mathrm{c}}}{f_k}\psi^{(\mathrm{c})}-\frac{f_k-f_{\mathrm{c}}}{f_k}\psi_{\mathrm{bs}}, \tag{10}$$

$$\mu_k=\frac{f_{\mathrm{c}}}{f_k}(\mu^{(\mathrm{c})}+\mu_{\mathrm{bs}})-\mu_{\mathrm{bs}}=\frac{f_{\mathrm{c}}}{f_k}\mu^{(\mathrm{c})}-\frac{f_k-f_{\mathrm{c}}}{f_k}\mu_{\mathrm{bs}}. \tag{11}$$

Proof The BS digital beamformer is designed to align with the BS–RIS channel, given by

$$\boldsymbol{v}_{\mathrm{D}}[k]=\sqrt{p[k]}\boldsymbol{b}^*(\vartheta,f_k),\ k=1,2,\ldots,K. \tag{12}$$

As such, according to Eqs. (5) and (7), the received signal in Eq. (9) can be written as

$$y[k]=\alpha[k]\boldsymbol{a}(\psi^{(\mathrm{c})},\mu^{(\mathrm{c})},f_k)\boldsymbol{Q}\boldsymbol{a}(\psi_{\mathrm{bs}},\mu_{\mathrm{bs}},f_k)s[k]+n[k], \tag{13}$$

where $\alpha[k]$ is a constant parameter. Below, we focus on the key part $\boldsymbol{a}(\psi^{(\mathrm{c})},\mu^{(\mathrm{c})},f_k)\boldsymbol{Q}\boldsymbol{a}(\psi_{\mathrm{bs}},\mu_{\mathrm{bs}},f_k)$ in Eq. (13) to configure the RIS. To direct the beam at the central frequency toward $(\psi^{(\mathrm{c})},\mu^{(\mathrm{c})})$, the RIS should be configured such that

$$\boldsymbol{Q}\boldsymbol{a}(\psi_{\mathrm{bs}},\mu_{\mathrm{bs}},f_{\mathrm{c}})=\boldsymbol{a}^*(\psi^{(\mathrm{c})},\mu^{(\mathrm{c})},f_{\mathrm{c}}). \tag{14}$$

When $\boldsymbol{Q}$ satisfies Eq. (14), i.e., the center-frequency beam is focused on $(\psi^{(\mathrm{c})},\mu^{(\mathrm{c})})$, the beam gain $\xi^{(\mathrm{c})}=|\boldsymbol{a}^{\mathrm{T}}(\psi^{(\mathrm{c})},\mu^{(\mathrm{c})},f_{\mathrm{c}})\boldsymbol{Q}\boldsymbol{a}(\psi_{\mathrm{bs}},\mu_{\mathrm{bs}},f_{\mathrm{c}})|$ reaches the maximum value 1. According to Eqs. (6) and (14), we find that $\varphi_n-2\pi\frac{f_{\mathrm{c}}}{c}(-\delta_n d\psi_{\mathrm{bs}}+\delta_n^2 d^2\mu_{\mathrm{bs}})-2\pi\frac{f_{\mathrm{c}}}{c}(-\delta_n d\psi^{(\mathrm{c})}+\delta_n^2 d^2\mu^{(\mathrm{c})})=0$ $(n=1,2,\ldots,N)$. Similarly, for the k^{th} subcarrier with frequency f_k, when $\hat{\psi}_k$ and $\hat{\mu}_k$ satisfy Eqs. (10) and (11), we can verify that the beam gain at $(\hat{\psi}_k,\hat{\mu}_k)$ reaches the maximum value, which implies that the beam at frequency f_k is focused on the location $(\hat{\psi}_k,\hat{\mu}_k)$.

As depicted in Fig. 3, when the bandwidth is large, the beam split effect leads to a significant deviation. The beams produced by subcarriers at the edge of the frequency band deviate from the center-frequency beam, in both the far field and the near field. Therefore, the beam split effect should be elaborately considered in subsequent codebook design and beam training.

3.2 Key ideas of codebook design

Building on the analysis of beam split, this subsection outlines the key ideas of codebook design for RIS-assisted OFDM communication systems.

According to Lemma 1, when configuring the RIS to align the beam at the central frequency toward a specific position, beams produced by subcarriers at other frequencies are directed toward nearby positions via beam split. Therefore, the coverage range of a wideband beam composed of multiple subcarrier beams surpasses that of a conventional narrow-band beam. This implies that fewer codewords are necessary to cover the near–far field, thereby reducing the overhead of beam training.

Note that while the coverage of codewords expands, the high angular and distance resolution can still be achieved. Given the orthogonality among OFDM subcarriers, the UE can distinguish signals at different frequencies. This is equivalent to further dividing a coverage-expanded codeword into coverage-refined codewords by using subcarriers of different frequencies. Coverage-refined codewords can

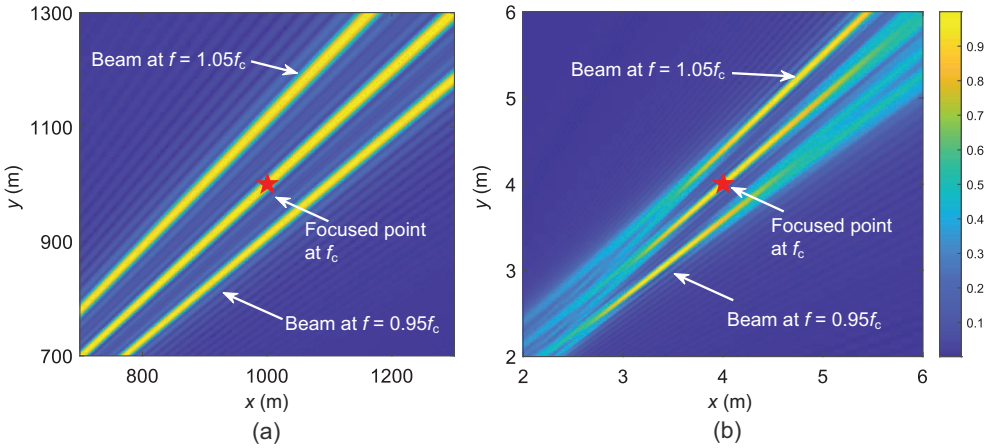

Fig. 3 Beam split in the far field (a) and the near field (b)

be regarded as a refined decomposition of coverage-expanded codewords, where each subcarrier beam's coverage is individually represented, reflecting the breakdown of the overall coverage across different subcarrier frequencies.

In summary, codewords that leverage the beam split effect, referred to as beam-split-aware codewords, can undergo two treatments. Initially, they are treated as coverage-expanded codewords to reduce codebook size and beam training overhead. Subsequently, they are treated as coverage-refined codewords to achieve superior angular and distance resolution.

3.3 Key ideas of beam training

We now introduce the key ideas of the beam training mechanism to be designed.

Considering the need for beam search across both angular and distance domains, an exhaustive approach would lead to significant time overhead. To address this issue, our approach involves initially conducting a preliminary angular search using only angular-domain codewords to estimate the potential angular range. Subsequently, more refined angular and distance searches are performed using coverage-expanded codewords within this narrowed range. It is worth noting that the coverage-expanded codeword can be decomposed into coverage-refined codewords via beam split, allowing for high resolution in terms of both angular and distance dimensions.

Additionally, due to the variations in channel gain across different subcarriers, conventional beam training schemes that rely on direct comparison of signal strengths are no longer effective. Therefore, we steer each subcarrier to the UE position as a single-frequency beam to estimate the channel gain across different subcarriers. By using the estimated channel gains of different subcarriers, we normalize the signal strength received by the UE during beam training. This eliminates the offset effect caused by frequency selectivity. As such, the normalized signal strength can more accurately reflect the angular and distance information of the channel between the RIS and the UE, leading to higher beam training accuracy.

4 Beam-split-aware codebook design for RIS

In this section, we describe our design of a beam-split-aware codebook capable of effectively covering the near–far field. We decompose the codebook design into angular sampling and distance sampling. After acquiring the position of sampling points, codewords are finally designed.

4.1 Angular sampling method

We first focus on the angular sampling method for codebook design. Angular sampling in the near–far field refers to sampling in the angular domain, involving the discretization of the angles within the near–far field region to obtain angular information of the sampling points. Specifically, when the center-frequency beam is directed to $\psi^{(\mathrm{c})}$, we determine the width of the wideband beam, composed of all subcarriers, by considering the angles ψ_1 and ψ_K

directed by beams at f_1 and f_K, respectively, where $f_1 = f_c - \frac{B}{2}$ and $f_K = f_c + \frac{B}{2}$. The angles ψ_1 and ψ_K can be obtained using Eq. (10).

In particular, in Eq. (10) we find that when $\psi^{(c)} = -\psi_{bs}$, i.e., the center-frequency beam is projected from the BS and reflected toward the user's direction in a mirror way in the ψ-domain, we have $\psi_k = \psi^{(c)}$ $(k = 1, 2, \ldots, K)$. In other words, the beams generated by subcarriers at different frequencies are directed toward the same direction when $\psi^{(c)} = -\psi_{bs}$, allowing us to treat it as a traditional narrow-band beam (Chen YH et al., 2023). The parameter w is introduced to represent the width of the wideband beam, and the angular coverage is $[\psi^{(c)} - \frac{w}{2}, \psi^{(c)} + \frac{w}{2}]$ when $\psi^{(c)} = -\psi_{bs}$. Without loss of generality, the width of the narrow-band beam is considered to be $\frac{2}{N}$ in the $\sin\theta$ plane (Lin et al., 2017; Chen YH et al., 2023). Therefore, in this paper, we set the value of w to $\frac{2}{N}$.

Drawing from the analysis, to ensure a comprehensive coverage of all angles while reducing the number of samples, we propose the following angular sampling method to construct the angular sampling set $\Psi^{(c)} = \{\psi_j^{(c)}\}$. As shown in Fig. 4, the angular sampling method we adopt involves iteratively updating the angular sampling set $\Psi^{(c)}$ and the coverage range $[\psi_{min}, \psi_{max}]$. We initialize with $\Psi^{(c)} = \{-\psi_{bs}\}$, where ψ_{bs} represents the angle of the BS in the ψ-domain. Given the fixed positions of the BS and RIS in practical communication systems, we assume that their relative positions are known, because they can be accurately determined using methods like minimum variance unbiased estimation, coordinate descent, and compressed sensing (Hu et al., 2021). The initial coverage range of the sampling set is $[-\psi_{bs} - \frac{w}{2}, -\psi_{bs} + \frac{w}{2}]$. We then iteratively expand the coverage toward $[-1, 1]$, which is the range of the ψ-domain. Specifically, given the current coverage range $[\psi_{min}, \psi_{max}]$, we calculate the next sampling angles toward -1 and 1, denoted as $\psi_-^{(c)}$ and $\psi_+^{(c)}$ respectively, ensuring no overlapping. These angles can be expressed as

$$\begin{cases} \psi_-^{(c)} = \frac{f_K}{f_c}(\psi_{min} + \psi_{bs}) - \psi_{bs}, \\ \psi_+^{(c)} = \frac{f_K}{f_c}(\psi_{max} + \psi_{bs}) - \psi_{bs}. \end{cases} \tag{15}$$

The sampling set $\Psi^{(c)}$ is then updated to $\{\psi_-^{(c)}, \Psi^{(c)}, \psi_+^{(c)}\}$. After adding $\psi_-^{(c)}$ and $\psi_+^{(c)}$ to $\Psi^{(c)}$, the current coverage range is also expanded, which can be obtained by using Eq. (10). The updated coverage range is $[\psi_{min}, \psi_{max}] = \left[\frac{f_c}{f_1}\left(\psi_-^{(c)} + \psi_{bs}\right) - \psi_{bs}, \frac{f_c}{f_1}\left(\psi_+^{(c)} + \psi_{bs}\right) - \psi\right]$. This process is iterated until $\psi_{min} \le -1$ and $\psi_{max} \ge 1$.

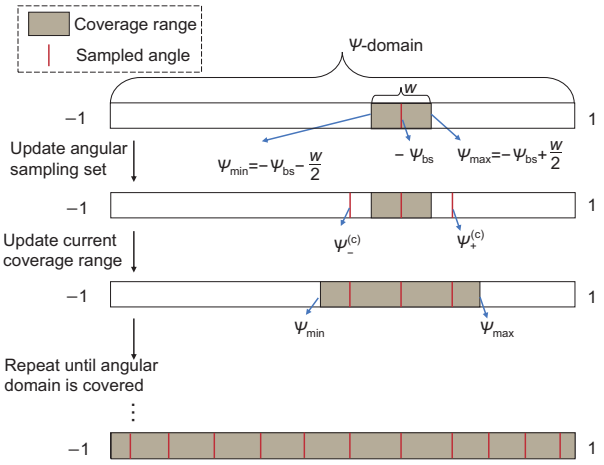

Fig. 4 Illustration of angular sampling

4.2 Distance sampling method

Next, we concentrate on the distance sampling method. Similar to angular sampling, distance sampling in the near–far field refers to sampling in the distance domain. For distance sampling, the column correlation is an important parameter used to characterize the relationship between adjacent sampling points (Cui and Dai, 2022; Zhang YP et al., 2022). Assuming that p and q are two adjacent sampling points at different distances from the same angle, their column correlation can be expressed as

$$G(\beta) = \left| \frac{\int_0^\beta \cos(\pi t^2/2)\mathrm{d}t + \mathrm{j}\int_0^\beta \sin(\pi t^2/2)\mathrm{d}t}{\beta} \right|, \tag{16}$$

where $\beta = \sqrt{\frac{D^2 f}{c}|\mu_p - \mu_q|}$ and D represents the antenna aperture. Given the maximum value of column correlation Δ, the function $G(\beta_\Delta) = \Delta$ can be used to determine β_Δ as

$$\beta_\Delta = G^{-1}(\Delta), \tag{17}$$

where $G^{-1}(\cdot)$ is the inverse function of $G(\cdot)$. To ensure that the column correlation between p and q remains below Δ, we require that $\beta_\Delta \le \sqrt{\frac{D^2 f}{c}|\mu_p - \mu_q|}$. This leads to the following criterion for distance sampling:

$$|\mu_p - \mu_q| \ge \frac{\beta_\Delta^2 c}{D^2 f}. \tag{18}$$

We now show that this distance sampling criterion can be generalized to the wideband case, as detailed in Lemma 2.

Lemma 2 If the distance between two adjacent beams at f_c satisfies $|\mu_p^{(c)} - \mu_q^{(c)}| \geq \frac{\beta_\Delta^2 c}{D^2 f_c}$, then the distance between adjacent beams at f_k also satisfies

$$|\mu_{p,k} - \mu_{q,k}| \geq \frac{\beta_\Delta^2 c}{D^2 f_k},\ k = 1, 2, \ldots, K. \tag{19}$$

Proof Using Eq. (11) and considering $|\mu_p^{(c)} - \mu_q^{(c)}| \geq \frac{\beta_\Delta^2 c}{D^2 f_c}$, the following can be obtained:

$$\begin{aligned} &|\mu_{p,k} - \mu_{q,k}| \\ &= \left|\left(\frac{f_c}{f_k}\mu_p^{(c)} - \frac{f_k - f_c}{f_k}\mu_{bs}\right) - \left(\frac{f_c}{f_k}\mu_q^{(c)} - \frac{f_k - f_c}{f_k}\mu_{bs}\right)\right| \\ &= \frac{f_c}{f_k}|\mu_p^{(c)} - \mu_q^{(c)}| \geq \frac{f_c}{f_k}\frac{\beta_\Delta^2 c}{D^2 f_c} = \frac{\beta_\Delta^2 c}{D^2 f_k}. \end{aligned} \tag{20}$$

Through Lemma 2, we find that when sampling the distance, we need only to control the column correlation between the sampling points of the central frequency f_c, as subcarriers at other frequencies automatically meet the aforementioned criteria after beam split. Therefore, given the maximum value of column correlation Δ, we can calculate β_Δ according to $|G(\beta_\Delta)| = \Delta$, and subsequently obtain the sampling distance set $\mathcal{U}^{(c)}$ via

$$\mathcal{U}^{(c)} = \{\mu_i^{(c)} | \mu_i^{(c)} = i\mu_\Delta^{(c)}, i = 0, 1, 2, \ldots\}, \tag{21}$$

where $\mu_\Delta^{(c)} = \frac{\beta_\Delta^2 c}{D^2 f_c}$.

4.3 Codeword design

Below, the codeword design approach is presented. Based on the angular and distance sampling methods, the position of each sampling point $(\mu_i^{(c)}, \psi_j^{(c)})$ can be determined in the near–far field. Consequently, we record the RIS configuration directed toward that point as its corresponding codeword $\boldsymbol{g}_{i,j}$ according to Eq. (14), which is expressed as

$$\boldsymbol{g}_{i,j} = \boldsymbol{a}^*(\psi_j^{(c)}, \mu_i^{(c)}, f_c) \oslash \boldsymbol{a}(\psi_{bs}, \mu_{bs}, f_c). \tag{22}$$

Following this, we calculate $\psi_{i,j,k}$ and $\mu_{i,j,k}$ using Eqs. (10) and (11) to record the distance and angle of the beam at f_k, i.e., the beam generated by the k^{th} subcarrier, for subsequent beam training. The proposed codebook design algorithm is outlined in Algorithm 1.

Algorithm 1 Beam-split-aware codebook design

Input: angular and distance sampling sets $\Psi^{(c)} = \{\psi_j^{(c)}\}$ and $\mathcal{U}^{(c)} = \{\mu_i^{(c)}\}$, subcarrier frequency set $\mathcal{F} = \{f_k\}$, central frequency f_c, and position of the BS (ψ_{bs}, μ_{bs}).

Output: codebook $\mathcal{G} = \{\boldsymbol{g}_{i,j}\}$, angular and distance arrays $\Psi = \{\psi_{i,j,k}\}$, and $\mathcal{U} = \{\mu_{i,j,k}\}$.

```
for μ_i^(c) ∈ U^(c) do
    for ψ_j^(c) ∈ Ψ^(c) do
        Construct the codeword g_{i,j} via Eq. (22)
        Record ψ_{i,j,k} via Eq. (10)  // Angular split
        Record μ_{i,j,k} via Eq. (11)  // Distance split
    end for
end for
```

Fig. 5 illustrates the coverage of the codewords within the proposed codebook in the $\psi - \mu$ domain. Note that when $i = 0$, $\boldsymbol{g}_{i,j}$ corresponds to the angular-domain codeword, i.e., the conventional far-field codeword. Additionally, in Fig. 5, we observe that subcarriers of different frequencies within a single codeword are further divided into different regions via beam split, indicating the

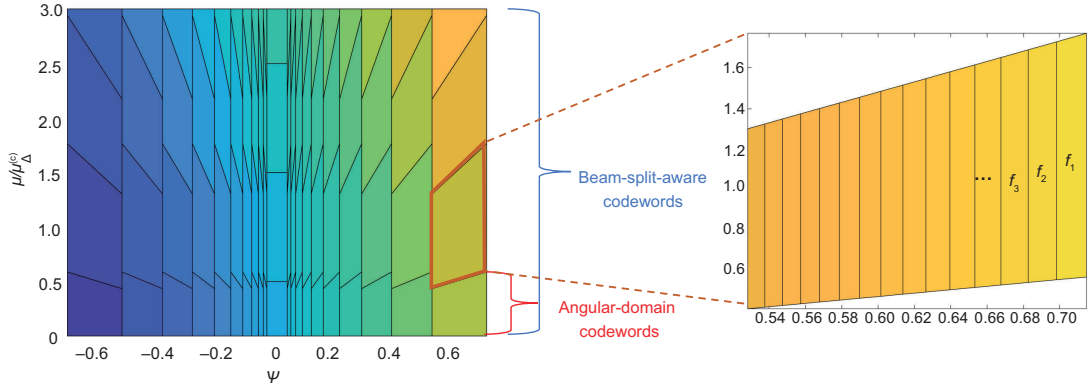

Fig. 5 Coverage range of beam-split-aware codewords ($\psi_{bs} = 0$)

potential for achieving high resolution in subsequent beam training.

5 Three-stage beam training mechanism

In this section, a three-stage beam training mechanism characterized by low training overhead is presented. We then extend the proposed scheme to multi-user scenarios.

Specifically, in the first stage, we determine the potential angular range by exclusively using angular-domain codewords for beam training. After that, in the second stage, an exhaustive search is conducted in the $\psi-\mu$ domain using near–far field codewords whose angle coverage range aligns with the potential angular range. Finally, in the third stage, we estimate the gain of each subcarrier and employ it to normalize the received power from the second stage, thereby obtaining the optimal codeword and estimating the UE's angular and distance information through the proposed beam training.

As stated before, considering the quasi-static property of the BS–RIS channel, we assume that the channel $\boldsymbol{H}_{\mathrm{br}}[k]$ is known by the system (Hu et al., 2021). Therefore, during beam training, we keep the digital beamformer $\boldsymbol{v}_{\mathrm{D}}[k]$ $(k=1,2,\ldots,K)$ to align with the BS–RIS channel according to Eq. (12). Below, we provide a detailed explanation of how each stage in the proposed three-stage beam training is performed.

5.1 First stage: potential angular range estimation

As shown in Fig. 6, in the first stage, the BS exclusively employs angular-domain codewords to configure the RIS, which means that $\boldsymbol{Q}$ is set as

$$\boldsymbol{Q}_{0,j}^{(1)}=\mathrm{diag}(\boldsymbol{g}_{0,j}),\ j=1,2,\ldots,J, \tag{23}$$

where J is the size of the angular sampling set $\Psi^{(\mathrm{c})}$. According to Eq. (9), the total received power of the UE can be expressed as

$$w_{0,j}^{(1)}=\sum_{k=1}^{K}||\boldsymbol{h}_{\mathrm{ru}}^{\mathrm{T}}[k]\boldsymbol{Q}_{0,j}^{(1)}\boldsymbol{H}_{\mathrm{br}}[k]\boldsymbol{v}_{\mathrm{D}}[k]s[k]+n[k]||^2. \tag{24}$$

Then, the index set of the codewords within the potential angular range, denoted by $\mathcal{J}^{(1)}$, is determined by

$$\mathcal{J}^{(1)}=\{\hat{j}^{(1)}|w_{0,\hat{j}^{(1)}}^{(1)}\geq\rho^2\max w_{0,j}\}, \tag{25}$$

where $\rho\in(0,1)$ represents the beam gain threshold. In particular, ρ can be set as $\frac{\sqrt{2}}{2}$, corresponding to the 3 dB dominant-angle region (Xiao et al., 2016).

5.2 Second stage: coarse direction and distance estimation

In the second stage, the BS uses beam-split-aware codewords whose angular coverage range aligns with the potential angular range for beam training. This is achieved by setting $\boldsymbol{Q}$ as

$$\boldsymbol{Q}_{i,j}^{(2)}=\mathrm{diag}(\boldsymbol{g}_{i,j}),\ i=1,2,\ldots,I,\ j\in\mathcal{J}^{(1)}, \tag{26}$$

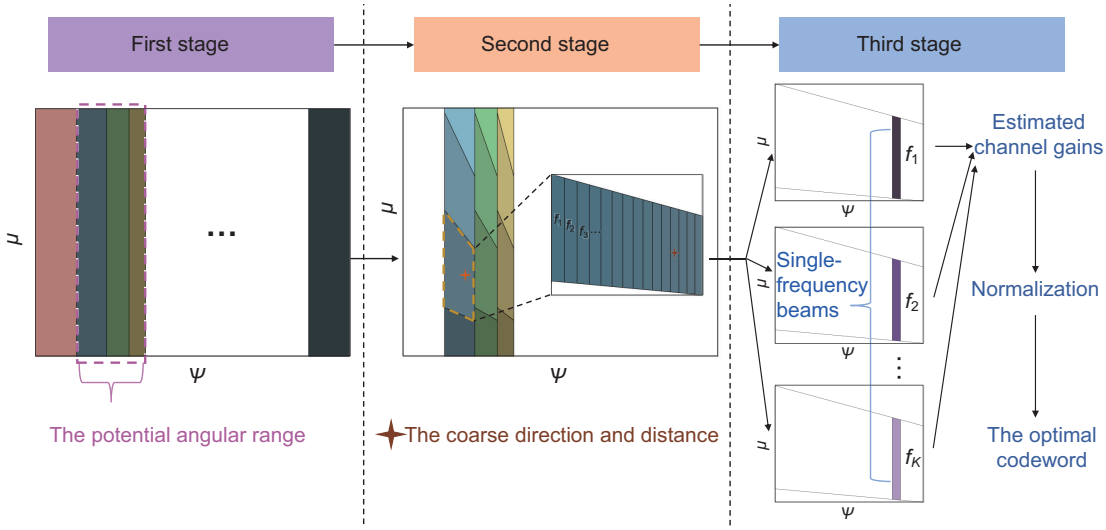

Fig. 6 Illustration of the proposed three-stage beam training mechanism

where I is the size of the distance sampling set $\mathcal{U}^{(\mathrm{c})}$. Different from the first stage, the UE records the received signal power of individual subcarriers $w_{i,j,k}^{(2)}$ instead of their total power, which is denoted as

$$w_{i,j,k}^{(2)} = ||\boldsymbol{h}_{\mathrm{ru}}^{\mathrm{T}}[k]\boldsymbol{Q}_{i,j}^{(2)}\boldsymbol{H}_{\mathrm{br}}[k]\boldsymbol{v}_{\mathrm{D}}[k]s[k] + n[k]||^2. \quad (27)$$

Next, the coarse estimated direction and distance of the UE, denoted as $(\hat{\psi}^{(2)}, \hat{\mu}^{(2)})$, can be obtained by

$$\begin{cases} (\hat{i}^{(2)}, \hat{j}^{(2)}, \hat{k}^{(2)}) = \arg\max w_{i,j,k}^{(2)}, \\ (\hat{\psi}^{(2)}, \hat{\mu}^{(2)}) = (\psi_{\hat{i}^{(2)},\hat{j}^{(2)},\hat{k}^{(2)}}, \mu_{\hat{i}^{(2)},\hat{j}^{(2)},\hat{k}^{(2)}}), \end{cases} \quad (28)$$

where the optimal index $(\hat{i}^{(2)}, \hat{j}^{(2)}, \hat{k}^{(2)})$ is determined by the UE and then transmitted to the BS. On the BS side, $(\hat{\psi}^{(2)}, \hat{\mu}^{(2)})$ is considered to be the element in Ψ and $\mathcal{U}$ corresponding to the index.

5.3 Third stage: channel gain estimation and normalization

In the third stage, the BS sequentially transmits single-frequency signals with frequencies corresponding to each subcarrier. It configures the RIS with

$$\boldsymbol{Q}_k^{(3)} = \mathrm{diag}(\boldsymbol{a}^*(\hat{\psi}^{(2)}, \hat{\mu}^{(2)}, f_k) \oslash \boldsymbol{a}(\psi_{\mathrm{bs}}, \mu_{\mathrm{bs}}, f_k)), \quad k = 1, 2, \ldots, K, \quad (29)$$

so that the beam is directed toward $(\hat{\psi}^{(2)}, \hat{\mu}^{(2)})$. The received power, denoted as $z[k]$, is recorded according to Eq. (9), which is used to normalize $w_{i,j,k}^{(2)}$ with

$$w_{i,j,k}^{(3)} = w_{i,j,k}^{(2)} / z[k]. \quad (30)$$

Finally, the optimal codeword $\hat{\boldsymbol{g}}$ and final estimated direction and distance of UE $(\hat{\psi}, \hat{\mu})$ are determined as follows:

$$\begin{cases} (\hat{i}, \hat{j}, \hat{k}) = \arg\max w_{i,j,k}^{(3)}, \\ \hat{\boldsymbol{g}} = \boldsymbol{g}_{\hat{i},\hat{j}}, \\ (\hat{\psi}, \hat{\mu}) = (\psi_{\hat{i},\hat{j},\hat{k}}, \mu_{\hat{i},\hat{j},\hat{k}}). \end{cases} \quad (31)$$

Note that the normalization and the comparison are performed by the UE, and that only the optimal index $(\hat{i}, \hat{j}, \hat{k})$ is transmitted to the BS. Then, according to the optimal index, the BS obtains $\hat{\boldsymbol{g}}$ and $(\hat{\psi}, \hat{\mu})$ for future data transmission.

The procedure of the proposed three-stage beam training mechanism is summarized in Algorithm 2.

Remark 1 For beam training, the complexity is primarily reflected in the beam training overhead, which refers to the number of time slots required.

Algorithm 2 Three-stage beam training mechanism

Input: codebook $\mathcal{G} = \{\boldsymbol{g}_{i,j}\}$, angular and distance arrays $\Psi = \{\psi_{i,j,k}\}$ and $\mathcal{U} = \{\mu_{i,j,k}\}$, and beam gain threshold ρ.

Output: optimal codeword $\hat{\boldsymbol{g}}$, estimated direction and distance of UE $(\hat{\psi}, \hat{\mu})$.

// First stage
for $\boldsymbol{g}_{0,j} \in \mathcal{G}$ **do**
  Transmit signals with $\boldsymbol{g}_{0,j}$
  Record the received power as $w_{0,j}^{(1)}$
end for
Obtain $\mathcal{J}^{(1)}$ via Eq. (25) // Potential angular range
// Second stage
for $i = 1 : I$ **do**
  for $j \in \mathcal{J}^{(1)}$ **do**
    Transmit signals with $\boldsymbol{g}_{i,j}$
    Record the received power as $w_{i,j,k}^{(2)}$
  end for
end for
Obtain $(\hat{\psi}^{(2)}, \hat{\mu}^{(2)})$ via Eq. (28) // Coarse estimation
// Third stage
for $k = 1 : K$ **do**
  Transmit single-frequency signals to $(\hat{\psi}^{(2)}, \hat{\mu}^{(2)})$
  Record the received power as $z[k]$
  Calculate $w_{i,j,k}^{(3)}$ via Eq. (30) // Normalization
end for
Obtain $\hat{\boldsymbol{g}}$ and $(\hat{\psi}, \hat{\mu})$ via Eq. (31)

The training overhead for an exhaustive search based on the proposed codebook is equivalent to the size of the proposed codebook, which is expressed as $\mathcal{O}(IJ)$. Letting S represent the number of angular-domain codewords within the potential angular range $\mathcal{J}^{(1)}$, the training overhead of three-stage beam training is given by $\mathcal{O}(J + SI + K)$. Since S is typically much smaller than J, the overhead of the latter is significantly reduced compared to that of the former, as demonstrated in Section 6.

5.4 Extension to multi-user scenarios

Similar to the existing two-phase beam training schemes (Zhang YP et al., 2022; Wu CY et al., 2024), the proposed framework is also applicable in multi-user scenarios by adopting TDMA. Below, we outline how the proposed scheme is extended to multi-user scenarios.

In the first stage, the BS exclusively employs angular-domain codewords to configure the RIS, with all UEs receiving signals simultaneously and recording the received power, similar to a single-user system. UEs then feed back the index sets of

codewords within the potential angular range to the BS in a time-division manner. The BS combines the potential angular ranges corresponding to each user $\mathcal{J}_u^{(1)}$ to determine the total potential angular range $\mathcal{J}^{(1)}$, given by

$$\mathcal{J}^{(1)} = \bigcup_{u=1}^{U} \mathcal{J}_u^{(1)}, \tag{32}$$

where U represents the number of UEs. In the second stage, the BS transmits signals using beam-split-aware codewords within the total potential angular range $\mathcal{J}^{(1)}$. UEs record the received power and feed back their own optimal index to the BS in a time-division manner. In the third stage, the BS transmits single-frequency signals to each UE based on the coarse estimates from the previous stage. UEs record the signal strength and feed back the corresponding index to the BS in a time-division manner.

6 Simulation results

In this section, simulation results are provided to validate the effectiveness of the proposed scheme. Specifically, we consider a RIS-assisted OFDM communication system with $M = 16$ BS antennas and $N = 128$ RIS elements. The central frequency is set as $f_c = 30$ GHz. The bandwidth is $B = 0.1 f_c = 3$ GHz with $K = 64$ subcarriers. The number of NLoS paths and Rician factor are, respectively, $L_{\mathrm{NLoS}} = 10$ and $\kappa = 30$ dB, which is practical in the mmWave frequency band (Liu W et al., 2023; Shi et al., 2024). The UE is assumed to be uniformly distributed within the region of $\theta \in (-\frac{\pi}{3}, \frac{\pi}{3})$ and $r \in (3, 100)$ m, i.e., the hybrid near–far field of the system. For comparison, the following schemes are performed as well:

1. Perfect CSI: The CSI is assumed to be perfectly known at the BS, which is considered as the upper bound.

2. Proposed codebook-based exhaustive beam training: Traverse all codewords in the proposed codebook.

3. Traditional near-field codebook-based exhaustive beam training: Using the angular and distance sampling method to construct the near-field codebook according to Cui and Dai (2022), traverse all codewords in the near-field codebook.

4. Two-phase near-field beam training (Zhang YP et al., 2022): The beam training is sequentially performed in the angular and distance domains based on the traditional near-field codebook.

5. Wideband far-field beam training (Chen YH et al., 2023): Develop an analytical beam training framework based on the power distribution pattern, which takes the wideband beam split effect in the far field into consideration.

Fig. 7 shows the beam training overhead versus the relative bandwidth. Compared to the near-field codebook, exhaustive beam training based on the proposed codebook brings a significantly reduced overhead, with a rapid decrease as the relative bandwidth increases. Benefiting from the staged beam training, the three-stage beam training based on the proposed codebook (proposed scheme) further reduces the training overhead. It can be observed that the overhead of the proposed scheme decreases with the reduction of the number of subcarriers, as the channel gain at the frequency of each subcarrier needs to be estimated in the third stage. Wideband far-field beam training searches solely in the angular domain, resulting in its low training overhead. However, subsequent simulations reveal that its performance in the near–far field is considerably worse compared to other schemes.

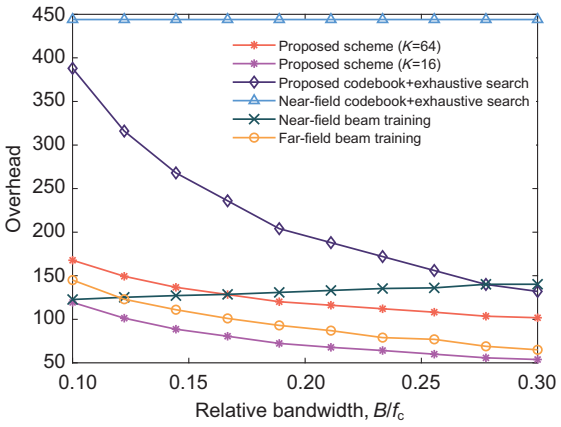

Fig. 7 Overhead vs. relative bandwidth

We compare the average angle estimation error versus SNR in Fig. 8, where the angle error is calculated using $\Delta\theta = |\arcsin\theta - \arcsin\hat{\theta}|$. The average error in the ψ-domain versus SNR is shown in Fig. 9, where the estimation error in the μ-domain is measured by $\Delta\mu = |\mu - \hat{\mu}|$. The estimation error of the high-overhead exhaustive search based on the proposed codebook is consistently lower than those of other schemes, which can be seen as the lower

bound. We observe that as the SNR increases, the proposed scheme can approach near-optimal performance with reduced overhead. The large angle error in the far-field scheme is due to its neglect of the spherical-wavefront channel characteristic in the near–far field. By leveraging the beam split effect to improve beam training resolution, the performance of two schemes based on the proposed codebook surpasses that of two schemes based on the traditional near-field codebook.

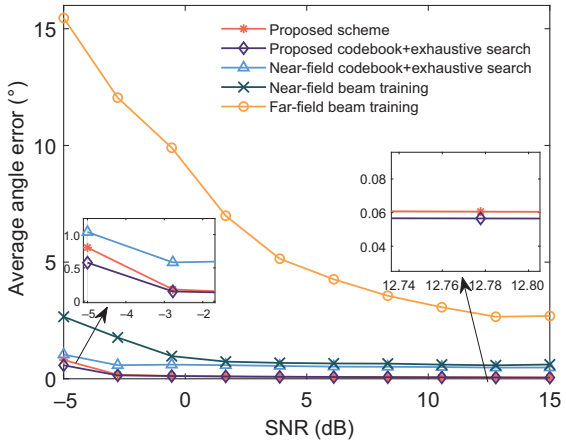

Fig. 8 Angle error vs. SNR

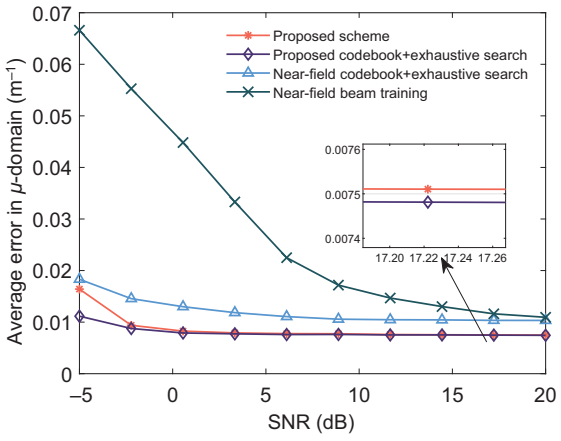

Fig. 9 Error in μ-domain vs. SNR

Fig. 10 presents the average angle estimation error of the proposed scheme versus the number of RIS elements N with different numbers of subcarriers K. The transmit SNR is set as 10 dB. It can be observed that the average angle error decreases as N increases. This is because a larger number of RIS elements produces narrower single-frequency beams, enabling more precise beam training during the second and third stages of the proposed mechanism. Additionally, as K increases, the average angle error gradually decreases, eventually to a steady value. Considering that the training overhead increases with the increase of K, there is a trade-off between the estimation error and training overhead (Zhang SP et al., 2023). In our simulation, we select $K = 64$ to achieve low estimation errors with reasonable overhead.

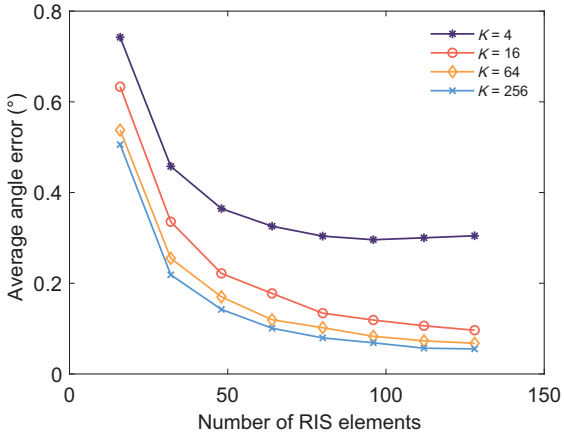

Fig. 10 Angle error vs. number of RIS elements

Fig. 11 illustrates the rate performance of different schemes versus the SNR. The sum rate is calculated as

$$R = \frac{1}{K}\sum_{k=1}^{K}\log_2\left(1+\frac{||\boldsymbol{h}_{\mathrm{ru}}^{\mathrm{T}}[k]\boldsymbol{Q}\boldsymbol{H}_{\mathrm{br}}[k]\boldsymbol{v}_{\mathrm{D}}[k]||^2}{\sigma^2}\right). \tag{33}$$

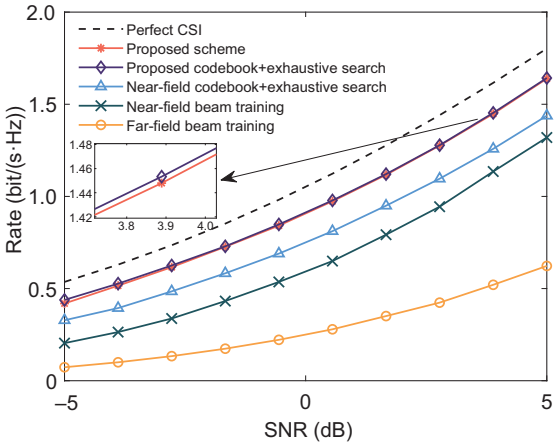

Fig. 11 Sum rate vs. SNR

During beamforming, the response matrix $\boldsymbol{Q}$ is obtained based on the estimated information $(\hat{\psi}, \hat{\mu})$,

which is expressed by

$$\boldsymbol{Q}=\mathrm{diag}(\boldsymbol{a}^{*}(\hat{\psi},\hat{\mu},f_{\mathrm{c}})\oslash\boldsymbol{a}(\psi_{\mathrm{bs}},\mu_{\mathrm{bs}},f_{\mathrm{c}})). \tag{34}$$

The digital beamformer $\boldsymbol{v}_{\mathrm{D}}$ is designed to align with the BS–RIS channel according to Eq. (12). The channels $\boldsymbol{h}_{\mathrm{ru}}[k]$ and $\boldsymbol{H}_{\mathrm{br}}[k]$ in the simulations are generated based on the channel model expressed by Eqs. (2) and (7), respectively. Note that the channel information here is used only in the simulations for sum rate performance evaluation. For our proposed scheme, the channel information $\boldsymbol{h}_{\mathrm{ru}}[k]$ is unknown, and thus we propose a three-stage beam training scheme to achieve beamforming without prior knowledge of CSI. It can be observed that as the SNR increases, the sum rate of the proposed three-stage beam training approaches that of exhaustive search, with a notable reduction in overhead. Benefiting from the high beam training resolution and accurate estimation of channel gains, the rate performance of the proposed codebook significantly outperforms that of traditional near-field and wideband far-field codebooks. The low rate performance of the near-field codebook stems from its neglect of the beam split effect, and the low rate performance of wideband far-field beam training results from its failure to account for the distance dimension and its inability to serve near-field users effectively.

Fig. 12 depicts the sum rate of the proposed scheme versus the number of OFDM subcarriers K. It can be observed that as K increases, the sum rate first increases and then decreases. The initial increase comes from the improved beam training accuracy supported by more subcarriers. The subsequent decrease implies that the performance enhancement benefiting from high beam training accuracy is lower than the performance degradation caused by beam split in beamforming (Mamat and Santipach, 2012). Additionally, we demonstrate how the limited RIS quantization bits for discrete phase shifts affect the performance of the proposed scheme. As the quantization resolution increases, the gap between the discrete phase case and the continuous phase case diminishes. The gap becomes negligible and near-optimal performance is achieved if the quantization resolution exceeds three bits.

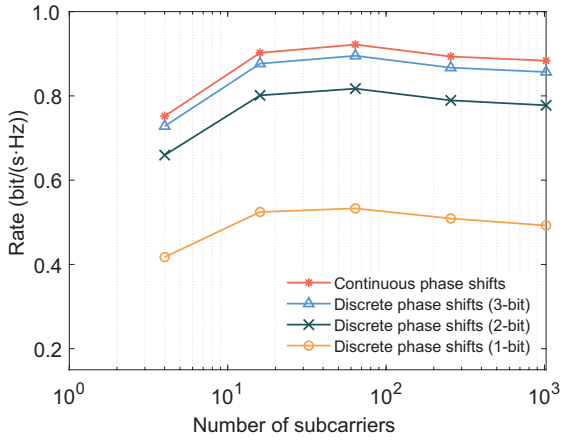

Fig. 12 Sum rate vs. number of subcarriers

7 Conclusions

In this paper, we investigate a RIS-assisted wideband OFDM communication system with unknown CSI of the user in the near–far field. Leveraging the beam split effect, we design a beam-split-aware codebook capable of covering the near–far field with fewer codewords compared to conventional narrow-band codebooks. Based on such a codebook, a three-stage beam training mechanism with low training overhead is proposed.

From simulation results, we draw the following conclusions: (1) Considering both near-field and far-field EM propagation characteristics, the proposed scheme is universally applicable to RIS-assisted near–far field wideband systems; (2) Benefiting from staged beam training, the proposed scheme significantly reduces training overhead compared to exhaustive search, while achieving comparable rate performance; (3) By taking into account the beam split effect, the proposed scheme outperforms conventional schemes in terms of the beam training resolution and sum rate.

Contributors

Boya DI designed the research. Zhichao CHENG and Shupei ZHANG processed the data and accomplished the simulation verification. Zhichao CHENG drafted the paper. Boya DI and Shu FU helped organize the paper. Zhichao CHENG and Shupei ZHANG revised and finalized the paper.

Conflict of interest

All the authors declare that they have no conflict of interest.

Data availability

The data that support the findings of this study are

available from the corresponding author upon reasonable request.

References

Basar E, di Renzo M, de Rosny J, et al., 2019. Wireless communications through reconfigurable intelligent surfaces. *IEEE Access*, 7:116753-116773. https://doi.org/10.1109/ACCESS.2019.2935192

Boljanovic V, Yan H, Lin CC, et al., 2021. Fast beam training with true-time-delay arrays in wideband millimeter-wave systems. *IEEE Trans Circ Syst I Reg Pap*, 68(4):1727-1739. https://doi.org/10.1109/TCSI.2021.3054428

Chen YH, Tan JB, Hao M, et al., 2023. Accurate beam training for RIS-assisted wideband terahertz communication. *IEEE Trans Commun*, 71(12):7425-7440. https://doi.org/10.1109/TCOMM.2023.3317291

Chen Z, Sun Z, Pei YK, et al., 2022. Generalized sparse codes for non-Gaussian channels: code design, algorithms, and applications. *Fundam Res*, 2(2):284-295. https://doi.org/10.1016/j.fmre.2021.12.006

Cheng Q, Jin S, Cui TJ, et al., 2023. Reconfigurable intelligent surfaces for wireless communications. *Front Inform Technol Electron Eng*, 24(12):1665-1668. https://doi.org/10.1631/FITEE.2320000

Cui MY, Dai LL, 2022. Channel estimation for extremely large-scale MIMO: far-field or near-field? *IEEE Trans Commun*, 70(4):2663-2677. https://doi.org/10.1109/TCOMM.2022.3146400

Cui MY, Dai LL, Wang ZC, et al., 2023. Near-field rainbow: wideband beam training for XL-MIMO. *IEEE Trans Wirel Commun*, 22(6):3899-3912. https://doi.org/10.1109/TWC.2022.3222198

Elayan H, Amin O, Shihada B, et al., 2020. Terahertz band: the last piece of RF spectrum puzzle for communication systems. *IEEE Open J Commun Soc*, 1:1-32. https://doi.org/10.1109/OJCOMS.2019.2953633

Gao FF, Xu LY, Ma SD, 2023. Integrated sensing and communications with joint beam-squint and beam-split for mmWave/THz massive MIMO. *IEEE Trans Commun*, 71(5):2963-2976. https://doi.org/10.1109/TCOMM.2023.3252584

Hu C, Dai LL, Han SF, et al., 2021. Two-timescale channel estimation for reconfigurable intelligent surface aided wireless communications. *IEEE Trans Commun*, 69(11):7736-7747. https://doi.org/10.1109/TCOMM.2021.3072729

Ju SH, Xing YC, Kanhere O, et al., 2021. Millimeter wave and sub-terahertz spatial statistical channel model for an indoor office building. *IEEE J Sel Areas Commun*, 39(6):1561-1575. https://doi.org/10.1109/JSAC.2021.3071844

Lin C, Li GY, Wang L, 2017. Subarray-based coordinated beamforming training for mmWave and sub-THz communications. *IEEE J Sel Areas Commun*, 35(9):2115-2126. https://doi.org/10.1109/JSAC.2017.2720038

Liu W, Pan CH, Ren H, et al., 2023. Low-overhead beam training scheme for extremely large-scale RIS in near field. *IEEE Trans Commun*, 71(8):4924-4940. https://doi.org/10.1109/TCOMM.2023.3278728

Liu YW, Liu X, Mu XD, et al., 2021. Reconfigurable intelligent surfaces: principles and opportunities. *IEEE Commun Surv Tutor*, 23(3):1546-1577. https://doi.org/10.1109/COMST.2021.3077737

Liu YW, Wang ZL, Xu JQ, et al., 2023. Near-field communications: a tutorial review. *IEEE Open J Commun Soc*, 4:1999-2049. https://doi.org/10.1109/OJCOMS.2023.3305583

Mamat K, Santipach W, 2012. Subcarrier clustering for MISO-OFDM channels with quantized beamforming. 9th Int Conf on Electrical Engineering/Electronics, Computer, Telecommunications and Information Technology, p.1-4. https://doi.org/10.1109/ECTICon.2012.6254267

Piesiewicz R, Kleine-Ostmann T, Krumbholz N, et al., 2007. Short-range ultra-broadband terahertz communications: concepts and perspectives. *IEEE Antenn Propag Mag*, 49(6):24-39. https://doi.org/10.1109/MAP.2007.4455844

Quan YH, Tian Z, Chen CZ, et al., 2023. Max-min rate optimization for multi-user MISO-OFDM systems assisted by RIS with a wideband model. *Front Inform Technol Electron Eng*, 24(12):1763-1775. https://doi.org/10.1631/FITEE.2300120

Salim OH, Nasir AA, Mehrpouyan H, et al., 2014. Channel, phase noise, and frequency offset in OFDM systems: joint estimation, data detection, and hybrid Cramér-Rao lower bound. *IEEE Trans Commun*, 62(9):3311-3325. https://doi.org/10.1109/TCOMM.2014.2345056

Selvan KT, Janaswamy R, 2017. Fraunhofer and Fresnel distances: unified derivation for aperture antennas. *IEEE Antenn Propag Mag*, 59(4):12-15. https://doi.org/10.1109/MAP.2017.2706648

Sherman J, 1962. Properties of focused apertures in the Fresnel region. *IRE Trans Antenn Propag*, 10(4):399-408. https://doi.org/10.1109/TAP.1962.1137900

Shi X, Wang JT, Sun Z, et al., 2024. Spatial-chirp codebook-based hierarchical beam training for extremely large-scale massive MIMO. *IEEE Trans Wirel Commun*, 23(4):2824-2838. https://doi.org/10.1109/TWC.2023.3303229

Shlezinger N, Dicker O, Eldar YC, et al., 2019. Dynamic metasurface antennas for uplink massive MIMO systems. *IEEE Trans Commun*, 67(10):6829-6843. https://doi.org/10.1109/TCOMM.2019.2927213

Suraweera HA, Armstrong J, 2004. Noise bucket effect for impulse noise in OFDM. *Electron Lett*, 40(18):1156-1157. https://doi.org/10.1049/el:20045825

Tang WK, Dai JY, Chen MZ, et al., 2020. MIMO transmission through reconfigurable intelligent surface: system design, analysis, and implementation. *IEEE J Sel Areas Commun*, 38(11):2683-2699. https://doi.org/10.1109/JSAC.2020.3007055

Tariq F, Khandaker MRA, Wong KK, et al., 2020. A speculative study on 6G. *IEEE Wirel Commun*, 27(4):118-125. https://doi.org/10.1109/MWC.001.1900488

Wang BL, Gao FF, Jin S, et al., 2018. Spatial-wideband effect in massive MIMO with application in mmWave systems. *IEEE Commun Mag*, 56(12):134-141. https://doi.org/10.1109/MCOM.2018.1701051

Wang X, Kong LH, Kong FX, et al., 2018. Millimeter wave communication: a comprehensive survey. *IEEE Commun Surv Tutor*, 20(3):1616-1653. https://doi.org/10.1109/COMST.2018.2844322

Wu CY, You CS, Liu YW, et al., 2024. Two-stage hierarchical beam training for near-field communications. *IEEE Trans Veh Technol*, 73(2):2032-2044. https://doi.org/10.1109/TVT.2023.3311868

Wu QQ, Zhang R, 2020. Towards smart and reconfigurable environment: intelligent reflecting surface aided wireless network. *IEEE Commun Mag*, 58(1):106-112. https://doi.org/10.1109/MCOM.001.1900107

Wu W, Liu DP, Hou XL, et al., 2020. Low-complexity beam training for 5G millimeter-wave massive MIMO systems. *IEEE Trans Veh Technol*, 69(1):361-376. https://doi.org/10.1109/TVT.2019.2926430

Xiao ZY, He T, Xia PF, et al., 2016. Hierarchical codebook design for beamforming training in millimeter-wave communication. *IEEE Trans Wirel Commun*, 15(5):3380-3392. https://doi.org/10.1109/TWC.2016.2520930

Yang SJ, Xie CF, Lyu WT, et al., 2024. Near-field channel estimation for extremely large-scale reconfigurable intelligent surface (XL-RIS)-aided wideband mmWave systems. *IEEE J Sel Areas Commun*, 42(6):1567-1582. https://doi.org/10.1109/JSAC.2024.3389120

Yue SH, Zeng SH, Zhang HL, et al., 2023. Intelligent omni-surfaces aided wireless communications: does the reciprocity hold? *IEEE Trans Veh Technol*, 72(6):8181-8185. https://doi.org/10.1109/TVT.2023.3242283

Yue SH, Zeng SH, Liu L, et al., 2024. Hybrid near-far field channel estimation for holographic MIMO communications. *IEEE Trans Wirel Commun*, 23(11):15798-15813. https://doi.org/10.1109/TWC.2024.3433491

Zhang HB, Zhang HL, Di BY, et al., 2022. Holographic integrated sensing and communication. *IEEE J Sel Areas Commun*, 40(7):2114-2130. https://doi.org/10.1109/JSAC.2022.3155548

Zhang SP, Zhang YT, Zhang HL, et al., 2023. Rate-overhead tradeoff for IOS-aided beam training: how large codebook is enough for the IOS? *IEEE Wirel Commun Lett*, 12(6):1081-1085. https://doi.org/10.1109/LWC.2023.3261968

Zhang YP, You CS, 2024. SWIPT in mixed near- and far-field channels: joint beam scheduling and power allocation. *IEEE J Sel Areas Commun*, 42(6):1583-1597. https://doi.org/10.1109/JSAC.2024.3389115

Zhang YP, Wu X, You CS, 2022. Fast near-field beam training for extremely large-scale array. *IEEE Wirel Commun Lett*, 11(12):2625-2629. https://doi.org/10.1109/LWC.2022.3212344

Zhang YT, Di BY, Zhang HL, et al., 2023. Near-far field beamforming for holographic multiple-input multiple-output. *J Commun Inform Netw*, 8(2):99-110. https://doi.org/10.23919/JCIN.2023.10173734